In Situ X-Ray Absorption Spectroscopic Study of Li$_{1.05}$Ni$_{0.35}$Co$_{0.25}$Mn$_{0.4}$O$_2$ Cathode Material Coated with LiCoO$_2$

Aniruddha Deb,[a,f,z] **Uwe Bergmann,**[b] **Stephen P. Cramer,**[c,d] and
Elton J. Cairns[a,e,*]

[a]*Environmental Energy Technologies Division and* [c]*Physical Bioscience Division, Lawrence Berkeley
National Laboratory, Berkeley, California 94720, USA*
[b]*Stanford Synchrotron Radiation Laboratory, Menlo Park, California 94025, USA*
[d]*Department of Applied Sciences, University of California, Davis, California 95616, USA*
[e]*Department of Chemical Engineering, University of California, Berkeley, California 94720, USA*

After the recent upsurge of interest in the layered LiNi$_{1/3}$Co$_{1/3}$Mn$_{1/3}$O$_2$ system for use as a cathode material for rechargeable lithium batteries, we have studied the charge compensation mechanism and structural perturbations occurring during cycling of the novel layered system of Li$_{1.05}$Ni$_{0.35}$Co$_{0.25}$Mn$_{0.4}$O$_2$ coated with nano-crystallized LiCoO$_2$, which effectively improved the rate capability. In addition, the LiCoO$_2$ evidently suppressed any structural change of the Li$_{1.05}$Ni$_{0.35}$Co$_{0.25}$Mn$_{0.4}$O$_2$. In situ X-ray absorption spectroscopy (XAS) measurements were performed utilizing a novel in situ electrochemical cell, specifically designed for long-term X-ray experiments. The cell was cycled at a moderate rate through a typical Li-ion battery operating voltage range (2.8–4.8 V). The electrode contained 1.9 mg of Li$_{1.05}$Ni$_{0.35}$Co$_{0.25}$Mn$_{0.4}$O$_2$ on a 25 μm Al foil, and had an area of 0.79 cm^2. XAS measurements were performed at different states of charge (SOC) during cycling, at the Ni, Co, and the Mn edges, revealing details about the response of the cathode to Li insertion and extraction processes. Extended X-ray absorption fine structure region of the spectra revealed the changes of bond distance and coordination number of Ni, Co, and Mn absorbers as a function of the SOC of the material. We found that the oxidation states of the transition metals in the system are Ni^{2+}, Co^{3+}, and Mn^{4+} in the fully discharged condition. During charging the Ni^{2+} is oxidized to Ni^{4+} through an intermediate stage of Ni^{3+}, Co^{3+} is oxidized almost to Co^{4+}. Utilizing a combination of Faraday's calculation and XAS results, the Co was found to be at Co$^{3.89+}$ at the end of the charge, whereas Mn was found to be electrochemically inactive and remains as Mn^{4+}. These measurements on this cathode material confirmed that the material retains its symmetry and good structural short-range order leading to superior cycling.
© 2007 The Electrochemical Society. [DOI: 10.1149/1.2720762] All rights reserved.

The search for environmentally friendly and cost effective lithium battery electrode materials with higher capacity and high cycling stability is an ongoing quest. With the emergence of portable telecommunications, computer equipment, and ultimately hybrid electric vehicles, there has been a great demand for substantial improvement in energy storage devices which can lead to less expensive batteries with longer lifetime and smaller size and weight. At present, the most commonly used commercial cathode material for the lithium-ion battery is LiCoO$_2$ due to its ease in production, stable electrochemical cycling, and acceptable specific capacity. But the relatively high cost of cobalt and the quest for materials with large capacity have led to the study of possible alternatives.

Lithium transition-metal oxides have always attracted attention as candidate electrode materials for lithium-ion batteries. Among them, layered LiTO$_2$ ($T = 3d$ transition metal element) materials with an α-NaFeO$_2$ structure have been widely investigated.[1] In recent years, there has been an upsurge in the search for technologically important new layered materials like LiNi$_{1/3}$Co$_{1/3}$Mn$_{1/3}$O$_2$. This system has been of significant interest and has been intriguing, as the Mn was found to be electrochemically inactive. This system can be considered as a special instance of Co substitution in the parent compound Li(Ni$_{1/2}$Mn$_{1/2}$)O$_2$,[2] with a chemical composition of Li(Ni$_x$Co$_{1-2x}$Mn$_x$)O$_2$, where $x = 1/3$. Moreover, a layered system LiNi$_{0.8}$Co$_{0.2}$O$_2$ has attracted attention as a new cathode material in lithium-ion batteries for hybrid electric vehicle applications. Compared to LiCoO$_2$, this system proved to possess enhanced electrochemical performance at a projected lower cost.[3]

Recently, a new layered cathode material of Li$_{1.05}$Ni$_{0.35}$Co$_{0.25}$Mn$_{0.4}$O$_2$ was studied in our laboratory,[4] with an α-NaFeO$_2$ structure, and delivering an initial discharge capacity of 165 and 195 mAh/g for the 2.8–4.5 and 2.8–4.8 V cutoff ranges. The discharge capacities at the 2.8–4.5 and 2.8–4.8 V decreased

with cycling and remained at 142 and 102 mAh/g after 20 cycles, which corresponds to 86% and 53% of their initial capacities.[4] Recent investigations have shown that the surface reaction of cathode materials strongly affects their electrochemical performance;[5] hence surface coatings with different metal oxides, e.g., Al$_2$O$_3$,[6] SnO$_2$,[7] have been successfully shown to retain the discharge capacity, and surface composition of the particles. Here in our laboratory, a coating of LiCoO$_2$ on this cathode material has been shown to increase the rate capability of this electrode. Hence, X-ray absorption spectroscopy (XAS) in situ experiments during cycling will be of immense importance and will be very informative in developing a complete understanding of the charge-discharge mechanism in this system. In the case of modern Li-ion batteries, the electrode materials permit lithiation and delithiation. This repeated insertion and removal of Li can cause significant volume changes that can result in severe degradation of the electrodes, strongly limiting the life time of the battery. Real-time tracking of the changes in the electrode materials undergoing electrochemical reactions is best performed by utilizing an in situ electrochemical cell. In situ XAS measurement is advantageous compared to ex situ measurements as it allows direct monitoring of the detailed structural changes in the electrode material as ion extraction/insertion proceeds. This, along with the simultaneous electrochemical measurements, provides unique, valuable information about the relationship between structure and electrochemical properties, which motivated the present experimental investigation.

Here, we apply transmission XAS to investigate Li$_{1.05}$Ni$_{0.35}$Co$_{0.25}$Mn$_{0.4}$O$_2$ electrodes (as used in Li-ion batteries) in various states of charge (SOC). Information about the valence state of the investigated transition metal elements (in our case, Mn, Co, and Ni) and their electronic configuration was obtained from the X-ray absorption near-edge spectroscopy (XANES) region of the K-absorption edges, whereas the extended X-ray absorption fine structure (EXAFS) region was used to probe the structure around the X-ray absorbing atoms. To the best of our knowledge there has been no in situ or ex situ XAS or X-ray diffraction (XRD) investigations reported on this novel system. It is important to mention here that we chose XAS as our tool as opposed to XRD. XRD gives one a

good picture of the long-range structural changes in the cathode, whereas in situ XAS investigations during cycling can be illuminating in their own right, providing an understanding of the oxidation state as well as short range ordering and providing a baseline for further studies in which the electrode material is modified by the introduction of additional elements. In addition, XAS can distinguish between the bulk properties (measurement in transmission mode) and surface properties (by fluorescence, or even more restricted to surface by electron yield or grazing incidence measurements). In this paper, we present a comprehensive analysis of Ni, Co, and Mn K-edge EXAFS, as well as an analysis of the XANES.
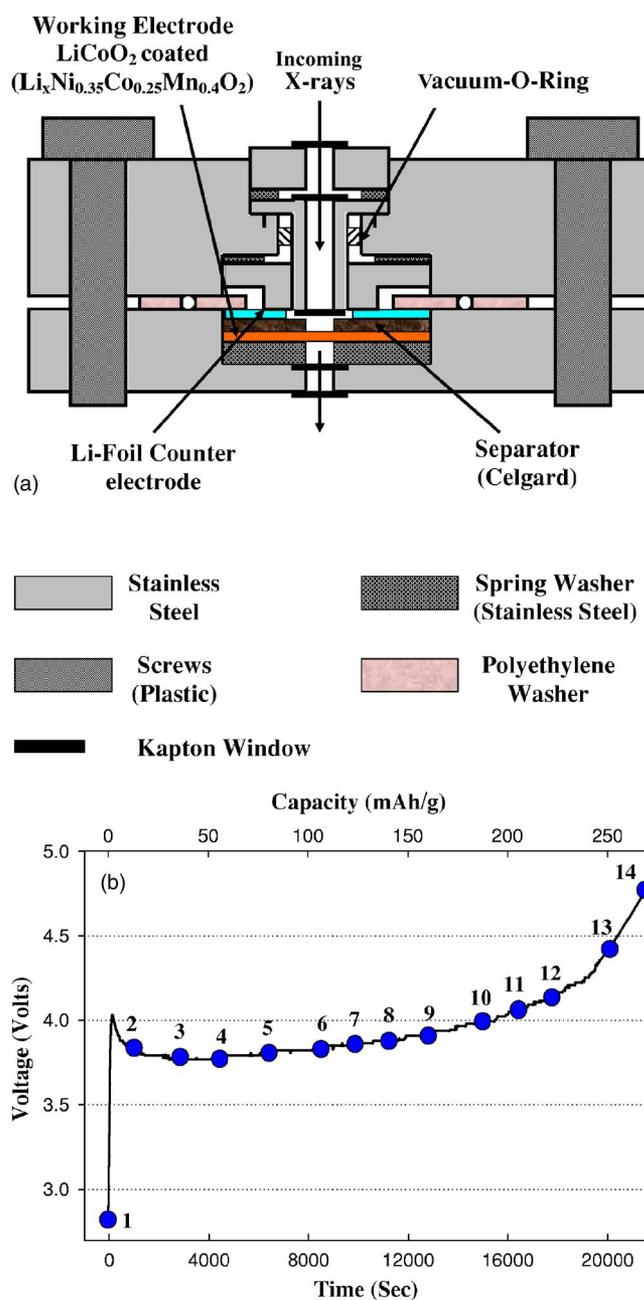
Experimental

The experiments were performed with a complete Li/LiCoO$_2$ coated Li$_{1.05}$Ni$_{0.35}$Co$_{0.25}$Mn$_{0.4}$O$_2$ cell. The prepared layered compound was single phase, as was verified by XRD. For a detailed description of the electrode preparation, the reader is referred to Son et al.[4] The electrochemical in situ XAS cell is shown in Fig. 1a. For a complete detailed electrochemical XAS cell design and assembly the reader is referred to Deb et al.[8] A sheet of porous polypropylene membrane (from Celgard, Celgard 3400) was utilized as a separator. The separator was punched with an outer diameter of 10 mm and an inner diameter of 4 mm. All of the necessary cell parts, along with the chemicals and tools for the assembly, were then placed in an argon-filled glove box in the laboratory. The separator was placed on top of the working electrode (LiCoO$_2$ coated Li$_{1.05}$Ni$_{0.35}$Co$_{0.25}$Mn$_{0.4}$O$_2$) (Fig. 1a). It was soaked with electrolyte 1 M LiPF$_6$ dissolved in 50 wt % ethylene carbonate (EC) and 50 wt % dimethylcarbonate (DMC) obtained as a solution from Merck Company. Finally, to complete the cell assembly, a piece of lithium foil counter electrode was then punched with an outer diameter of 10 mm and an inner diameter of 6 mm from fresh supplies and placed on top of the separator. A computer-controlled Princeton Applied Research model VERSA potentiostat/galvanostat was used for cycling the electrochemical cell under constant current control.

In situ XAS measurements performed during charging and discharging were carried out at various states of charge of the electrode. Charging and discharging were performed at a constant current density of 0.09 mA/cm^2 between 2.8 and 4.8 V, which corresponds to about the 6 h rate (or 0.09 mA/cm^2 for 6 h, raising the potential to 4.8 V) (Fig. 1b). The charging was paused during the XAS measurements. The spectra presented here were obtained during the charging process at different states of charge (100% SOC corresponds to 4.8 V vs Li).

For measurements with the model compounds, they were diluted with boron nitride (BN), and 0.78 cm^2 pellets were pressed using a pressure of 9 tons, yielding pellets about 400 μm thick. Pellets were mounted on aluminum sample holders using Kapton adhesive foil on both sides of the sample for measurements.
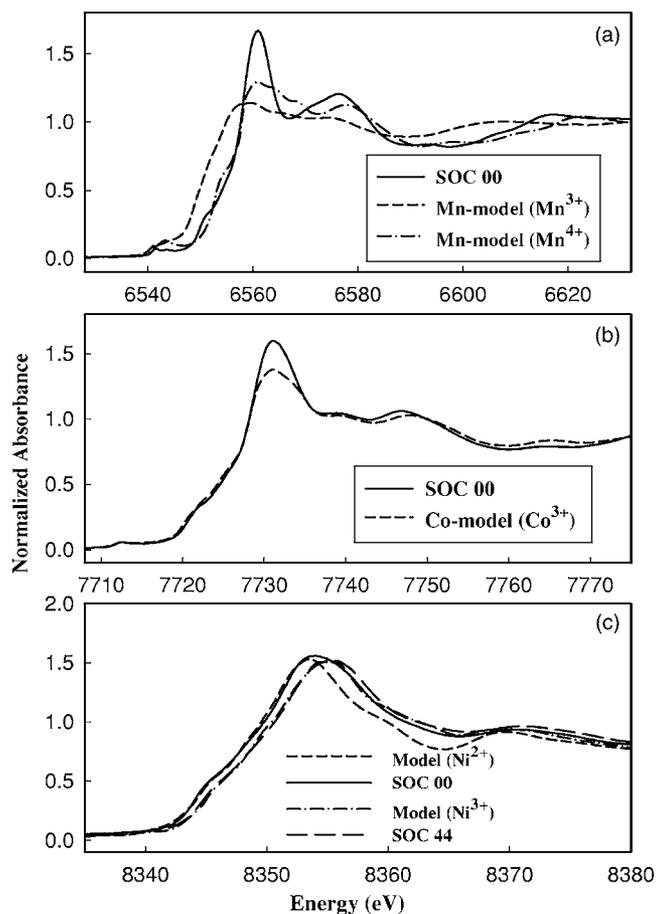
The XAS measurements were performed at the bending magnet beamline station D of the DuPont-Northwestern-Dow Collaborative Access Team (DND-CAT) at the Advanced Photon Source, Argonne National Laboratory. A Si(111) water-cooled double crystal monochromator was used, where the resolution of the monochromatic beam was determined to be 1.0 eV. The I_0 (incident signal) and the I_t (transmitted signal) chambers were filled with a helium-nitrogen mixture (15/85% and 11/89%, respectively), whereas the I_{ref} (reference signal) chamber was filled with a mixture of nitrogen and argon (82/18%). To allow the X-ray beam to easily pass through the electrochemical reaction cell a beam size of 0.33 × 0.5 mm was chosen, with an incident photon flux of ~10^{11} photons/s. For the Mn K absorption edge the monochromator was scanned from 200 eV below to 800 eV above the edge, whereas for the Ni K edge the energy scan was from 6539 to 8333 eV, and the data range collected at the Co K-absorption edge was limited to 8250 eV (12.7 Å^{-1}) by the onset of the Ni K edge. Data were collected within this energy range, with a step size of 0.2 eV in the respective edge region. The energy calibrations at each edge were performed using Mn, Co, and

Ni metal foils between the I_t and I_{ref} ion chambers, respectively. XAS spectra were collected at each of these absorption edges. EXAFS data reduction was performed using the Exafspak software package[9] and Athena.[10] The resulting $\chi(k)$ function was then weighted with k^3 to compensate for the damping of oscillations with increasing k. The radial structure functions were obtained by Fourier transformation of $k^3\chi(k)$ using a k range of 1.5–16.2 Å^{-1} for Mn and Ni and 1.5–12.7 Å^{-1} for Co.

The XRD pattern of the bare (uncoated) and the material coated with LiCoO$_2$ were studied. The coated material does not show any change in structure. Both samples exhibit a well defined α-NaFeO$_2$ structure with no minor phases. Distinct splitting of the [(108), (110)] and [(006), (102)] peaks were observed. Thus, the atomic

Figure 1. (Color online) (a) Schematic view of the in situ XAS electrochemical cell. (b) Voltage profile of the in situ XAS electrochemical cell during the first charge. The XAS scans are measured at the points indicated in the voltage profile.

Figure 2. Calibrated and normalized XANES comparison of (a) Mn K edge for $Li_{1.05}Ni_{0.35}Co_{0.25}Mn_{0.4}O_2$, observed at 0% SOC with the model compound Mn_2O_3 (Mn^{3+}) (broken line) and MnO_2 (Mn^{4+}) (dash-dot line), (b) Co K edge for $Li_{1.05}Ni_{0.35}Co_{0.25}Mn_{0.4}O_2$, observed at 0% SOC with the model compound $LiCoO_2$ (Co^{3+}), and (c) Ni K edge for $Li_{1.05}Ni_{0.35}Co_{0.25}Mn_{0.4}O_2$, observed at 0% SOC (thick solid line) and 44% SOC (thick broken line) with the model compounds nickel (II) oxide (Ni^{2+}) (broken line) and $LiNi_{0.8}Co_{0.2}O_2$ (Ni^{3+}) (dash-dot line), respectively.

structure fits the space-group symmetry of R3 m (α-NaFeO$_2$) type, ITC no. 166 (International Tables for X-Ray Crystallography). The structure has Li ions at the 3a sites, the transition metal ions (M = Mn, Co, and Ni) at the 3b sites, and O ions at the 6c sites in a hexagonal setting. For the coated material the lattice parameters "a" and "c" decreased by about 0.3% with respect to the uncoated material, which suggests that the phase on the surface of the powder is LiCoO$_2$ crystals formed by the coating process. TEM images of the coated material showed a coating thickness of 10–30 nm particle size, as a uniform film on the cathode material. For a detailed description of the characterization of the coated sample the reader is referred to Son and Cairns.[4]

Results and Discussion

In general, the shape of the K-edge XANES of the transition metal oxides provides unique information about the site symmetry and the nature of the bonding with surrounding ligands, while the threshold energy position of the absorption edge provide information about the oxidation state of the probed atom. To extract the information of the initial oxidation state of the transition metals in this material we here present in Fig. 2 the XANES regions at 0% SOC compared to model compounds at the Mn, Co, and Ni edges, respectively. The qualitative difference is immediately apparent from the figures. A comparison of the Mn K-edge XANES spectrum

in Fig. 2a of $Li_{1.05}Ni_{0.35}Co_{0.25}Mn_{0.4}O_2$, with model compounds Mn_2O_3 (Mn^{3+}) and MnO_2 (Mn^{4+}), reveals that the edge energy is essentially the same as that of MnO_2 (Mn^{4+}), indicating that the oxidation state of Mn in this material at start (0% SOC) is nearly all tetravalent (Mn^{4+}). Due to charge balance considerations for this material, it is likely that a small fraction of the Mn is in a charge state of +3. The comparison of the XANES spectrum for the sample at the Co K edge with that of $LiCoO_2$, shown in Fig. 2b, indicates that the XANES spectrum for the Co K edge of the sample is identical to that of $LiCoO_2$ (Co^{3+}), indicating that Co in the sample at 0% SOC is at Co^{3+}. Finally, XANES spectrum for the sample at the Ni K edge was compared with those of two model compounds of Nickel (II) oxide [NiO (Ni^{2+})] and layered $LiNi_{0.8}Co_{0.2}O_2$ (Ni^{3+}), shown in Fig. 2c. Comparison to the Ni^{3+} model compound was mainly performed to confirm if there was any intermediate stage of Ni^{3+} during the cycling procedure. The XANES spectrum for the Ni K edge of the sample is similar to that of Nickel (II) oxide, indicating that Ni in $Li_{1.05}Ni_{0.35}Co_{0.25}Mn_{0.4}O_2$ is divalent (Ni^{2+}) at 0% SOC, whereas the Ni K-edge XANES is similar to that of layered $LiNi_{0.8}Co_{0.2}O_2$ at 44% SOC, confirming that Ni in this system is trivalent (Ni^{3+}) at 44% SOC.

XANES spectra for selected SOC values at the Mn, Co, and Ni edges during the charging process are shown in Fig. 3. Mn K-edge XANES (Fig. 3a) edge position of the first six scans at different charge states did not exhibit any significant edge shift to higher energies, suggesting that the Mn oxidation state during the charging process remains unchanged, i.e., the Mn^{4+} atom is electrochemically inactive. While the XANES observed for the Co K edge (Fig. 3b) shows a progression of the entire pattern from lower energy to higher energy as a function of the decreased Li content (at the five different charge states), indicating the oxidation of Co^{3+} towards Co^{4+} (almost to Co^{4+} as it will be shown in the following section), and the XANES spectra for the Ni K edge are shown in Fig. 3c. Ni K edge shows a two-stage change during charging, where the first stage is from 0% SOC to 44% SOC and the second stage is from 44% SOC to 79% SOC. Above 79% SOC, the XANES spectrum of the Ni K edge did not move noticeably to a higher energy. This two-stage observation may be attributed to the two one-electron reactions of the Ni ions (Ni^{2+}/Ni^{3+} and Ni^{3+}/Ni^{4+}) during charging. It is important to mention here that similar observations have recently been reported by Koyama et al.[11] using ab initio calculations, that the redox reaction in a similar layered system of $Li_{1-x}Ni_{1/3}Co_{1/3}Mn_{1/3}O_2$ (where the transition metals are in different compositions from the present system) consists of Ni^{2+}/Ni^{3+}, Ni^{3+}/Ni^{4+}, and Co^{3+}/Co^{4+}, where the redox reaction were found to be in the ranges of $0 \leq x \leq 1/3$, $1/3 \leq x \leq 2/3$, and $2/3 \leq x \leq 1$, respectively. During discharge, we observed that these processes are reversed electrochemically: Li is inserted in the lattice structure, the Co^{4+} and Ni^{4+} are reduced to Co^{3+} (trivalent) and Ni^{2+} (divalent) states, and the M(metal)-O and M-M bond lengths almost return to their original values. Hence only the data during the charging half-cycle has been presented here for discussion.

It is important to note here that the shapes of the absorption edges for Ni in the various states of charge cannot be reconstructed by a linear combination of the Ni^{4+} and Ni^{2+} edge contributions. For example, Fig. 3d shows a comparison of the spectrum calculated by linear combination of the Ni^{2+} and Ni^{4+} spectra and the spectrum for 44% SOC. The important areas of mismatch are the concave downward feature at 8341 eV, and the absorption maximum. The feature at 8341 eV is characteristic of Ni^{3+}, and is absent from the calculated edge spectrum; the mismatch in the absorption maximum is an additional indication of the presence of Ni^{3+} instead of a combination of Ni^{2+} and Ni^{4+}. This is strong and clear evidence for the existence of Ni^{3+} as an intermediate state for the Ni in its oxidation/reduction cycling.

The nature of the pre-edge region of the respective XAS spectra for the transition metals observed during cycling are shown in the insets of Fig. 3a-c, respectively. The pre-edge results provide addi-
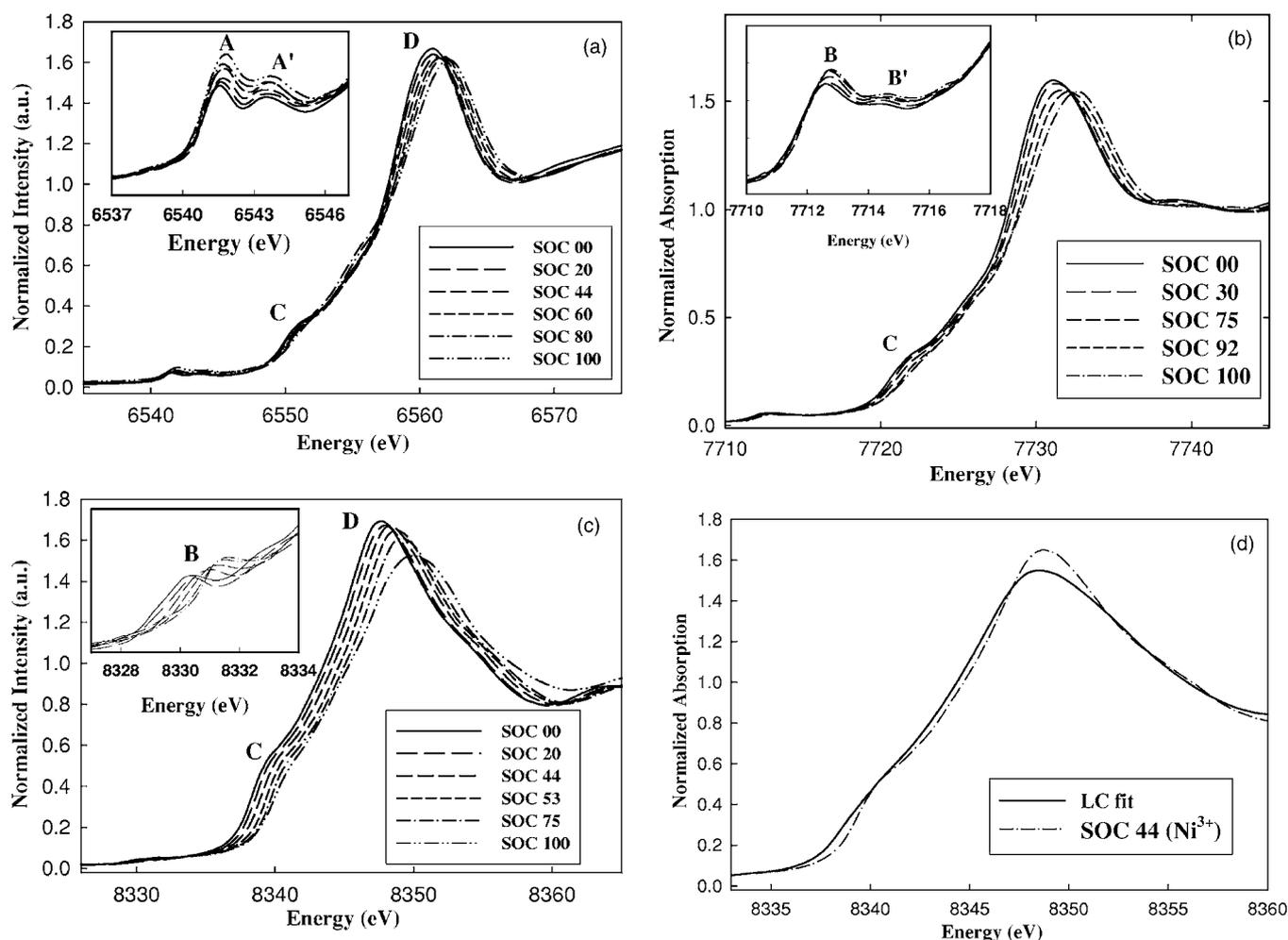
Figure 3. Calibrated and normalized XANES spectra for $Li_{1.05}Ni_{0.35}Co_{0.25}Mn_{0.4}O_2$ at different states of charge at the (a) Mn K edge, (b) Co K edge, and (c) Ni K edge, respectively. The insets show the nature of the pre-edge peaks of the respective XAS spectra. (d) Comparison of the linear combination (LC) fit of the Ni^{2+} (0% SOC) and Ni^{4+} (100% SOC) spectra (with a composition of 43%, 0% SOC and 57%, 100% SOC states) with the 44% SOC spectra.

tional insight about the nature of the electronic states. For most transition elements, the pre-edge peaks are seen to occur well below the main edge (~ 15 eV below) and these are assigned to transitions to empty states with d-like character [1s to $3d^{(n+1)}$] transitions,[12,13] where n represents the initial number of d electrons while ($n + 1$) includes the excited electron in the final state, which usually includes the effect of a core hole. These $1s \rightarrow 3d$ transitions are directly allowed through a very weak quadrupole transition[14] or allowed via an admixture of 3d and 4p states.[15] In the inset, of Fig. 3a, the pre-edge region for Mn in all the spectra recorded during delithiation exhibits two peaks structure denoted by A and A$'$ (~ 6542 and ~ 6544 eV), are assigned as the transitions from the core 1s level to unoccupied 3d states which are, in turn, electric dipole forbidden. The mixing of the p-orbital into 3d orbitals can also contribute to the pre-edge intensity, which has much higher intensity than the electric quadrupole-allowed transition. Thus, even though this transition is dipole forbidden, the pre-edge peaks here could be discerned due to quadrupole-allowed transitions and/or due to the mixing of the 4p and 3d states. The observation of a weak intensity of the pre-edge here is indicative of the octahedral coordination as opposed to the tetrahedral coordination where strong pre-edge intensity is observed.[16] The observation of a two peak structure here for Mn (A and A$'$) in the pre-edge indicates manganese is in the tetravalent state, as a pre-edge with only one peak characteristic feature is observed for trivalent manganese compounds. This characteristic single-peak pre-edge feature for trivalent manganese com-

pounds as discussed by Horne et al.,[17] is interpreted as a result of the splitting of the t_{2g} and e_g energy levels modified by Jahn-Teller deformation. In the case of Co XANES spectra shown in Fig. 3b, are mainly from the Co $1s \rightarrow 3d$ transitions, and are not well structured here, but it clearly shows two edges (B and B$'$) with some weak indication of an energy splitting in between, assigned to the 1s $\rightarrow t_{2g}$ and $1s \rightarrow e_g$ transitions. The presence of the two transitions indicates at least a partial high-spin configuration, while as the peaks are not clearly split, it may be due to the delocalized electrons in the band structure or an overlapping mixture of low-spin $^1A_1(t_{2g}^6e_g^0)$, intermediate $^3T_1(t_{2g}^5e_g^1)$, and high-spin $^5T_3(t_{2g}^4e_g^2)$ states. Transitions from 1s to the t_{2g} orbitals are both symmetry and dipole forbidden, but they do occur, albeit very weakly, due to the mixing with the oxygen p orbitals and quadrupole transitions. On the other hand, transitions from 1s to e_g orbitals are also dipole forbidden, and hence also much weaker than the symmetry- and dipole-allowed $1s \rightarrow 4p$ main transition. The shoulder C observed at ~ 7222 eV represents the shake-down process in which $1s \rightarrow 4p$ transition with ligand $\rightarrow$ 3d electron transition or ligand to metal charge transfer (LMCT) [$1s^1c3d^6 \rightarrow 1s^1c3d^7L$] occurs. The binding energy decrease due to the core-hole screening effect in Co by an electron transferred in from a ligand, leads to the transition in the shake-down process at a lower energy.[18] The pre-edge in the Ni K edge spectrum (shown in Fig. 3c) is almost absent during the charging process, which leads to the conclusion that the local environment of
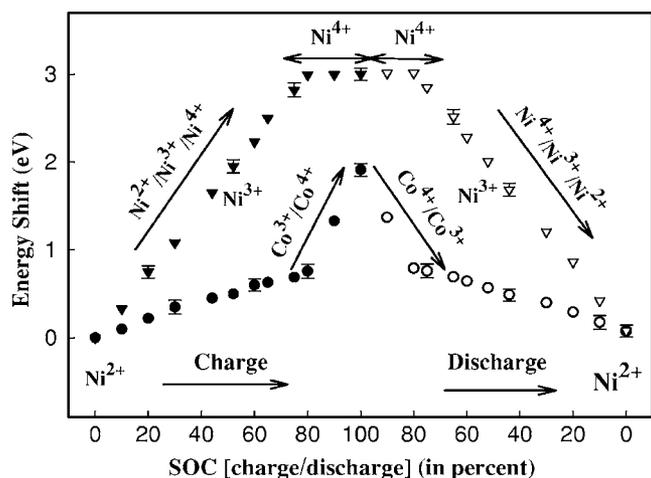
Figure 4. Plot of the white line energy shift vs the state of charge (SOC) for Co and Ni K edge. The filled symbols (▼ and ●) represent the data during charging, while the empty symbols (▽ and ○) represent the data during discharging.

the Ni atoms is highly symmetrical during the charging process, as a nonsymmetrical octahedral local environment will lead to a higher $1s \rightarrow 3d$ peak intensity.[19]

Figure 4 shows a quantitative picture of how the redox process is changing during the cycling process, where we have shown the change in the white line peak position as a function of the SOC as opposed to the edge position, defined by the energy at half of the edge step for the Co, and the Ni K edge, observed during delithiation and lithiation. The Co and the Ni peak positions change by +1.92 and +3.1 eV, respectively, as the lithium content changes from the OCV fully discharged state to the fully charged (4.8 V vs Li) state. The Co oxidation state in the system is observed to be changing and nearly proportional to the SOC [except after 78% SOC where there is an increase in slope (Fig. 4) which is consistent with our Faraday's law calculation (Fig. 5)]. It is not possible with this transmission method to distinguish between the Co in the coating and in the bulk material. The values reported are overall averages. The Ni edge in the system seems to go through a two-step change (from 0% SOC to 44% SOC and from 44% SOC to 78% SOC),
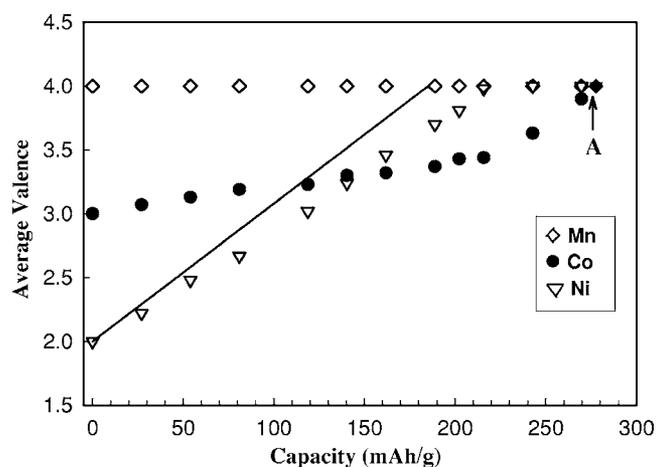
Figure 5. Average valence vs capacity profiles for the first charge of the cell for the transition metals Ni (▽), Co (●), and Mn (◇). The average valence of Ni (▼) and that of Mn (♦) at the theoretical calculated capacity (277 mAh/g) have been shown here as position A. The solid line is the guide to the eye using Faraday's law considering that all the charge is used for changing the nickel valence from Ni^{2+} to Ni^{4+}.

which may be attributed to the two-electron reaction of Ni ions as discussed earlier. Above 78% SOC the Ni edge does not change significantly, suggesting that Ni^{2+} is fully oxidized to Ni^{4+}, while charge compensation still occurs in Co (Fig. 4).

Now relating our XAS findings with electrochemistry a quantitative analysis was performed using the Faraday's law. Utilizing Faraday's law the total theoretical capacity of the coated material under consideration here is 277.63 mAh/g, hence, theoretically for each of the three redox changes for the transition metals in the system (i.e., Ni^{2+} to N^{3+}, Ni^{3+} to Ni^{4+}, and Co^{3+} to Co^{4+}) during cycling can be achieved by using one-third of the total theoretical capacity, i.e., 92.54 mAh/g. Hence, utilizing the information of the experimentally measured capacity at each state of the charging process, together with the average valence change from the XAS results (Fig. 4) and the theoretical capacity, the average Ni and Co valence can be represented as

$$Ni_{val} = 2.0 + \left[\frac{\text{Exp. measured capacity(mAh/g)}}{92.54 \text{ mAh/g}} \right] \times (Ni_{frac})$$

[1]

$$Co_{val} = 3.0 + \left[\frac{\text{Exp. measured capacity(mAh/g)}}{92.54 \text{ mAh/g}} \right] \times (Co_{frac})$$

[2]

and

$$Ni_{frac} + Co_{frac} = 1 \qquad [3]$$

where the Ni_{val} and Co_{val} represent the average Ni and Co valence during the cycling procedure and Ni_{frac} is the fraction of the charge that causes change in the Ni valence and Co_{frac} is the fraction of the charge that causes change in the Co valence.

The XAS results show that the Ni^{2+} at the start changes to Ni^{3+} at 44% SOC (118 mAh/g) and finally changes to Ni^{4+} at 78% SOC (210 mAh/g). Hence, Ni_{frac} can be obtained by using Eq. 1, and using the Co_{frac} value from Eq. 3, the Co_{val} can be obtained from Eq. 2. This quantitative information is shown in Fig. 5, where we can see that during the first charge cycle the Co is almost changed from Co^{3+} to Co^{4+}. Figure 5 shows that at the theoretical capacity of 277.63 mAh/g Mn is Mn^{4+} and Ni is Ni^{4+}, while we found that at the measured extraction capacity of the first cycle (221 mAh/g) Mn is Mn^{4+}, Ni is Ni^{4+}, and Co is $Co^{3.89+}$. The line in Fig. 5 shows the guidance from Faraday's law on how the Ni valence changes if all of the charge is used to change the Ni valence only. The observed increase in slope of the Co K-edge white line in Fig. 4 after 78% SOC can now be explained by the Faraday's law results in Fig. 5. This increase in slope is due to the fact that after 78% SOC Ni is at Ni^{4+}, and the whole of the charge is now used to change the valence of Co, as can be seen from Fig. 5.

The local structure of the Mn, Co, and Ni ions in $Li_{1.05}Ni_{0.35}Co_{0.25}Mn_{0.4}O_2$ was obtained from EXAFS measurements. The backgrounds were subtracted by extrapolating a Victoreen-type function from the pre-edge region, and EXAFS oscillations $\chi(k)$ were extracted using cubic spline baseline functions.[20] In all cases, the Li contribution to the XAFS was ignored because of the low backscattering ability of the lithium. The normalized $k^3\chi(k)$ function for selected scans at different SOC values during the charging cycle, as a function of $k(\text{Å}^{-1})$ for Mn, Co, and Ni are shown in Fig. 6. Only small changes take place in the case of Co and Ni between the different SOC values. This can be more clearly understood from the results of the FT (Fourier transform) of the data at selected SOC's, as shown in Fig. 7-9. Here, Ni EXAFS extends to a k value of 15 Å^{-1}, but the Co EXAFS extends to only 12.5 Å^{-1}, due to the presence of the Ni edge at 8.33 keV. The first peak at 1.9 Å in Fig. 7-9 is attributed to the Mn–O, Co–O, and Ni–O interactions, respectively. It is observed that during cycling Mn–O distance remains nearly unchanged, contrary to the gradual dwindling of the Co–O distances and the decrease of the
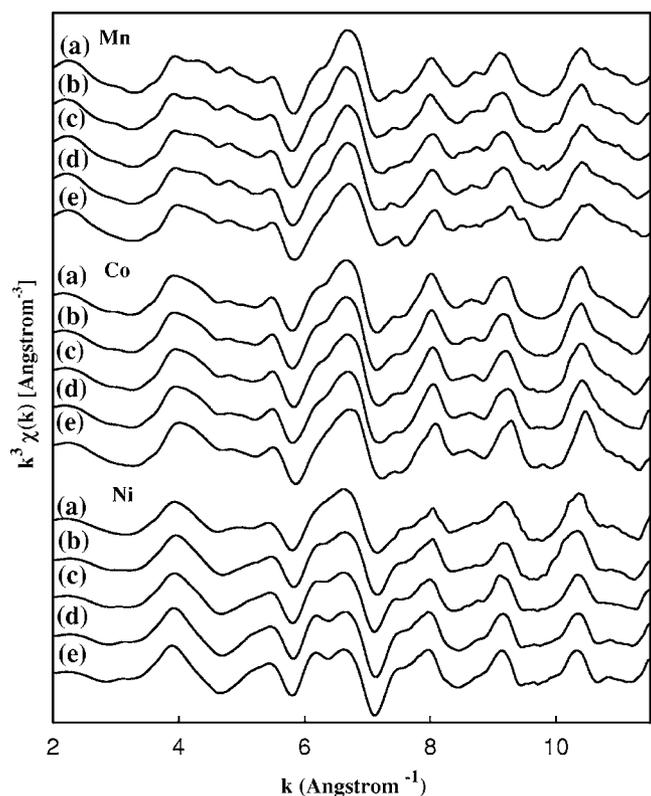
Figure 6. Selected $k^3\chi(k)$ data observed for Mn at (a) 0% SOC, (b) 20% SOC, (c) 44% SOC, (d) 80% SOC, and (e) 100% SOC, for Co at (a) 0% SOC, (b) 30% SOC, (c) 75% SOC, (d) 92% SOC, and (e) 100% SOC, and for Ni K edges at (a) 0% SOC, (b) 20% SOC, (c) 44% SOC, (d) 75% SOC, and (e) 100% SOC.

Ni–O distances, which can be related to the change in the valence state in the transition metals. In the octahedral crystal field, the d orbitals split into triply degenerate (t_{2g}) and a higher-energy doubly
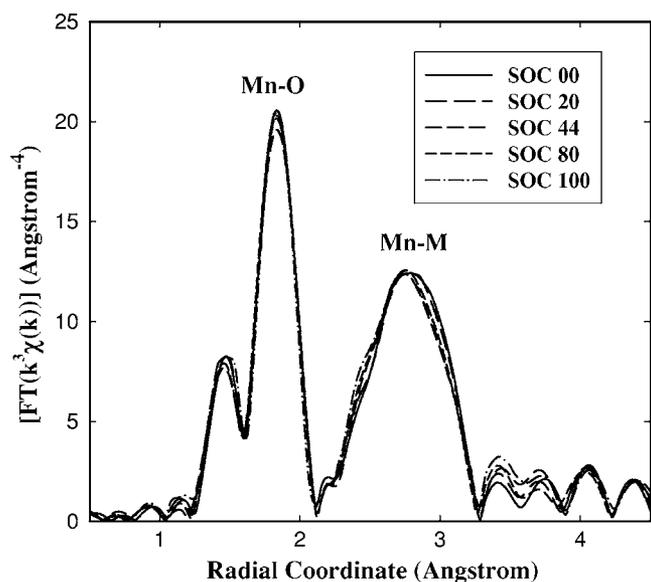
Figure 7. Magnitude of the k^3-weighted Fourier transform of $Li_{1.05}Ni_{0.35}Co_{0.25}Mn_{0.4}O_2$ at the Mn K edge at selected SOC during the charge cycle (k range = 1.5–15.1 Å^{-1}). M represents the transition metal atom.
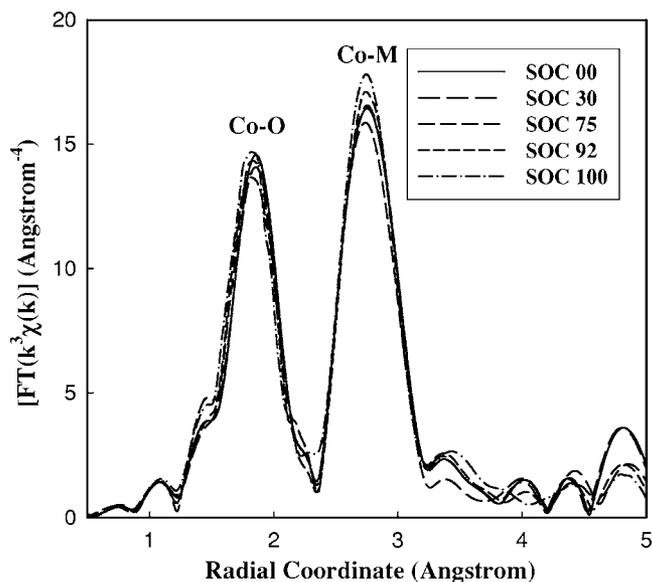
**Figure 8.** Magnitude of the k^3-weighted Fourier transform of $Li_{1.05}Ni_{0.35}Co_{0.25}Mn_{0.4}O_2$ at the Co K edge at selected SOC during the charge cycle (k range = 1.5–12.5 Å^{-1}). M represents the transition metal atom.

degenerate set (e_g), which leads to an outermost electronic configuration for Co^{3+}/Co^{4+} as $t_{2g}^6 e_g^0/t_{2g}^5 e_g^0$, while for Ni^{2+}/Ni^{4+} (or Ni^{3+}/Ni^{4+}) as $t_{2g}^6 e_g^2/t_{2g}^6 e_g^0$ (or $t_{2g}^6 e_g^1/t_{2g}^6 e_g^0$). The change in energy during the Co^{3+}/Co^{4+} redox reaction is small as the change takes place only in the t_{2g} degenerate set, which results in a very small change in the ionic radius ($R_{Co}^{3+} \sim 0.54$ Å/$R_{Co}^{4+} \sim 0.53$ Å), whereas the variation in energy for Ni^{2+}/Ni^{4+} (or Ni^{3+}/Ni^{4+}), where the change takes place between the lower t_{2g} and higher e_g sets, would be larger, inducing a larger change in the ionic radius (R_{Ni}^{2+}
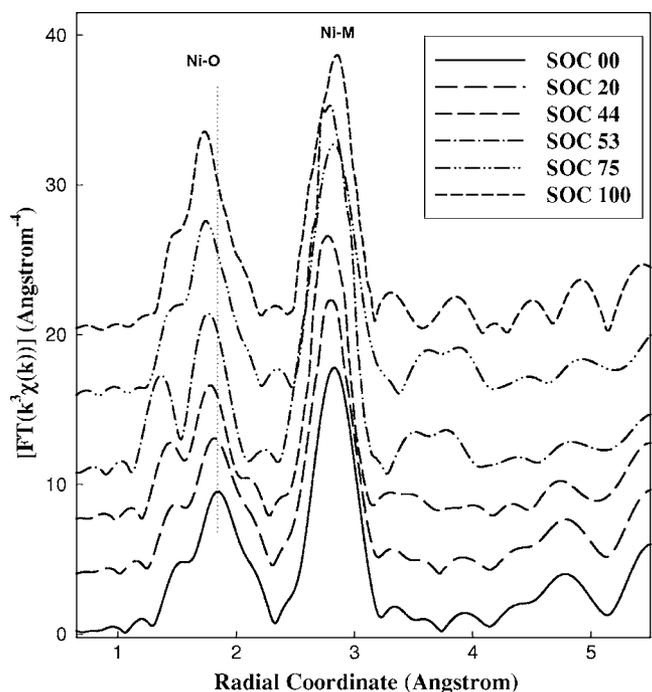

Figure 9. Magnitude of the k^3-weighted Fourier transform of $Li_{1.05}Ni_{0.35}Co_{0.25}Mn_{0.4}O_2$ at the Ni K edge at selected SOC during the charge cycle (k range = 1.5–15.1 Å^{-1}). M represents the transition metal atom.
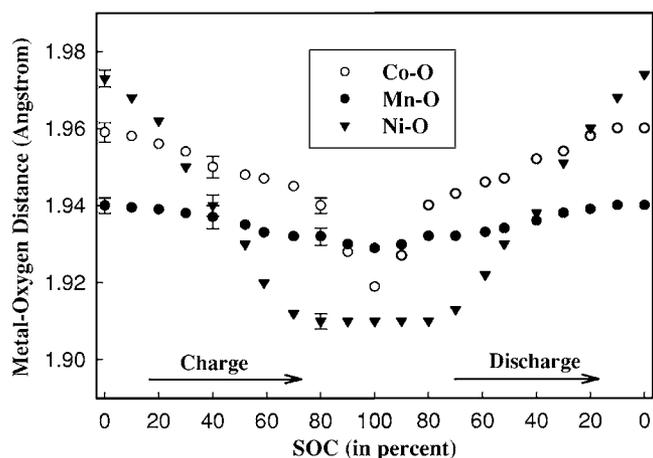
Figure 10. First shell metal-oxygen coordination bond length changes during Li/Li$_{1.05}$Ni$_{0.35}$Co$_{0.25}$Mn$_{0.4}$O$_2$ cell cycling. The filled symbols (● and ▼) represent the Mn–O and Ni–O bond distances, while the empty symbol (○) represents the Co–O bond distances as observed during different states of charge and discharge.

Figure 11. Second shell metal-metal coordination bond length changes during Li/Li$_{1.05}$Ni$_{0.35}$Co$_{0.25}$Mn$_{0.4}$O$_2$ cell cycling. The filled symbols (▼ and ●) represent the Mn–M and Ni–M bond distances, while the empty symbol (○) represents the Co–M bond distances as observed during different states of charge and discharge.

~ 0.69 Å/$R_{Ni}^{3+} \sim 0.56$ Å/$R_{Ni}^{4+} \sim 0.48$ Å). Unlike Li$_{1-x}$Ni$_{0.5}$Co$_{0.5}$O$_2$[21] and Li$_{1-x}$NiO$_2$[22] here, as the sample is delithiated it can be seen that the amplitude of the Ni–O and the Co–O peaks almost remains the same. These observations can be best understood by considering the local structure of Ni and Co in pure LiNiO$_2$ and LiCoO$_2$. For LiNiO$_2$ as studied earlier,[23] oxygen atoms are present at two different distances surrounding Ni, where the distorted octahedral coordination is consistent with a Jahn-Teller effect expected for Ni^{3+} in a low-spin state. For Li$_{1-x}$NiO$_2$ system during delithiation the increase of the Ni–O peak amplitude has been ascribed to the changes in the local structure of the Ni created by the oxidation of the Ni^{3+} to Ni^{4+} and because Ni^{4+} is not a Jahn-Teller active ion, the oxidation of Ni^{3+} to Ni^{4+} results in a diminution of the Jahn-Teller effect which results in an increased amplitude of the Ni–O peak. Li$_{1-x}$CoO$_2$ system during delithiation does not exhibit any increase of the Co–O peak, which has been ascribed to the absence of the Jahn-Teller effect in the case of Co^{3+}. Based on these observations, we conclude that the absence of a Jahn-Teller active ion (i.e., Co^{3+} and Ni^{2+} are not Jahn-Teller active ions) results in a similar amplitude for the Ni–O and the Co–O interactions in the FT during delithiation. The second peak at ~ 2.8 Å in Fig. 7-9 arises due to a metal-metal interaction, where the Co and the Ni edges the peak positions shift to lower R values as Li is deintercalated. Previously, in pure LiNiO$_2$,[21] similar behavior was observed by Nakai and Nakagome for the Ni–Ni interaction.

An analysis of the structural parameters of the Mn, Co, and Ni absorbers was performed based on a two shell model, obtained by nonlinear least-squares fits to the first two peaks of the FT spectra at the K edges of Mn, Co, and Ni, respectively. The bond distances (R) and the Debye-Waller factors (σ) were left as free parameters, and the coordination number (CN) of Mn–O, Co–O, Ni–O, Mn–M, Co–M, and Ni–M was kept fixed to the crystallographic value of six (summarized in Fig. 10 and 11). The first shell metal-oxygen (Mn–O, Co–O, and Ni–O) interaction distances at various charge and discharge states are shown in Fig. 10, where it is evident that the Mn–O distances varied the least (at the most ~ 0.009 Å), while the Co–O distances varied by ~ 0.035 Å and the Ni–O distances varied the most, by ~ 0.06 Å. We observed for Ni–O distances above 78% state of charge, the change in the distance is negligible and is ~ 0.001 Å; this is consistent with the fact that after 78% SOC in the system the Ni^{2+} is changed fully to Ni^{4+} (shown in Fig. 4). The relatively bigger decrease in the Ni–O bond distance can be interpreted by the oxidation of Ni^{2+} to Ni^{4+} because the ionic radius of Ni^{2+} (0.69 Å) is larger than that of Ni^{4+} (0.46 Å).[24] Moreover, bond
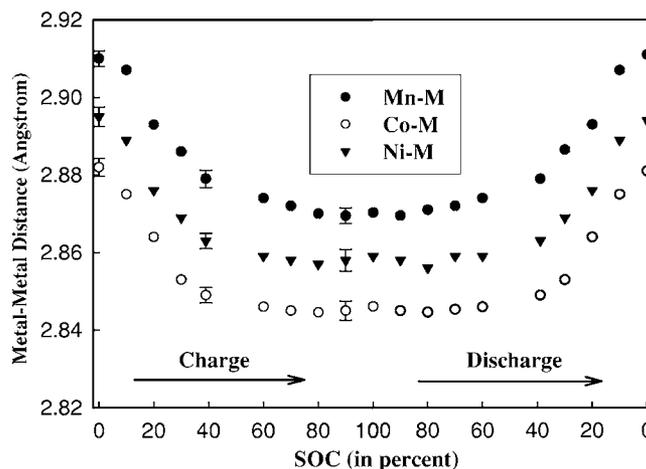
distance of Ni^{4+}–O in this system (~ 1.87 Å) is consistent with other previously reported Ni^{4+}–O bond distances observed in compounds such as BaNiO$_3$ and KNiIO$_6$ (~ 1.88 Å),[25,26] which clarifies that at the end of the charge Ni^{2+} is completely oxidized to Ni^{4+}. Finally, the metal-metal (Mn–M, Co–M, and Ni–M) interaction distances at various charge and discharge states are shown in Fig. 11, where the changes in M–M distances at the Mn, Co, and Ni K edges between the initial and the fully charged state varies at the most by 0.04 Å (0.03 Å for Mn–M, 0.04 Å for Co–M, and 0.050 Å for Ni–M) about 1.4% contraction. These metal-metal distances correspond to the a lattice parameter of the trigonal $R3m$ cell where the metal-metal distances are consistent with the changes seen in the case of X-ray diffraction pattern for this system.[4]

Conclusions

XAS characterization of this system during charging and discharging cycles provided us with an excellent tool for analyzing the changes that occur when Li is cycled into and out of the layered lattice. XANES results confirm that during the charging to 4.8 V, the oxidation state of Mn does not change and remains tetravalent (Mn^{4+}) until the end of charging and was found to be electrochemically inactive, whereas divalent nickel (Ni^{2+}) is oxidized to tetravalent nickel (Ni^{4+}), passing through an intermediate stage of trivalent nickel (Ni^{3+}). The cobalt is found to be oxidized from Co^{3+} to almost Co^{4+} during the entire range of the state of charge as confirmed from Faraday's law results. Small volumetric changes and the retention of its hexagonal lattice structure confirm that this material possesses very desirable characteristics for an electrode, which makes it an excellent choice for Li-ion cell applications.

References

1. R. Koksbang, J. Barker, H. Shi, and M. Y. Saidi, *Solid State Ionics*, **84**, 1 (1996).
2. A. Deb, U. Bergmann, S. P. Cramer, and E. J. Cairns, *J. Appl. Phys.*, **99**, 063701 (2006).
3. X. Zang P. N. Ross, Jr., R. Kostecki, F. Kong, S. Sloop, J. B. Kerr, K. Striebel, E. J. Cairns, and F. McLarnon, *J. Electrochem. Soc.*, **148**, A463 (2001).
4. (a) J. T. Son and E. J. Cairns, *Electrochem. Solid-State Lett.*, **9**, A27 2006; (b) J. T. Son and E. J. Cairns, *J. Power Sources*, **166**, 343 (2007).
5. J. T. Son, G. S. Park, H. T. Chung, and H. G. Kim, *J. Power Sources*, **126**, 182 (2004).
6. J. Cho, J.-G. Lee, B. Kim, and B. Park, *Chem. Mater.*, **15**, 3190 (2003).
7. Z. Wang, X. Huang, and L. Chen, *J. Electrochem. Soc.*, **150**, A199 (2003).
8. A. Deb, U. Bergmann, E. J. Cairns, and S. P. Cramer, *J. Synchrotron Radiat.*, **11**, 497 (2004).
9. G. N. George and I. J. Pickering, Exafspak, Stanford Synchrotron Radiation Laboratory, Stanford, CA, (1993).
10. M. Newville, *J. Synchrotron Radiat.*, **8**, 322 (2001).
11. Y. Koyama, I. Tanaka, H. Adachi, Y. Makimura, and T. Ohzuku, *J. Power Sources*, **119–121**, 644 (2003).
12. J. S. Griffith, *The Theory of Transition Metal Ions*, Cambridge University Press, Cambridge, England (1961).
13. S. Sugano, Y. Tanabe, and H. Kamimura, *Multiplets of Transition-Metal Ions*, Vol. 1, p. 73, Academic, New York (1970).
14. (a) A. Manceau, A. I. Gorshkov, and V. A. Drits, *Am. Mineral.*, **77**, 1133 (1992);

(b) B. Poumellec, V. Kraizman, Y. Aifa, R. Cortes, A. Novakovich, and R. Vedrinskii, *Phys. Rev. B*, **58**, 6133 (1998); (c) O. Sipr, A. Simunek, S. Bocharov, T. Kirchner, and G. Drager, *Phys. Rev. B*, **60**, 14115 (1999).
15. J. E. Hahn, R. A. Scott, K. O. Hodgson, S. Doniach, S. R. Desjardins, and E. I. Solomon, *Chem. Phys. Lett.*, **88**, 595 (1982).
16. (a) M. Belli, A. Scafati, A. Bianconi, S. Mobilio, L. Palladino, A. Reale, and E. Burattini, *Solid State Commun.*, **35**, 355 (1980); (b) A. Manceau, A. I. Gorshkov, and V. A. Drits, *Am. Mineral.*, **77**, 1133 (1992).
17. C. R. Horne, U. Bergmann, M. M. Grush, R. C. C. Perera, D. L. Ederer, T. A. Callcott, E. J. Cairns, and S. P. Cramer, *J. Phys. Chem. B*, **104**, 9587 (2000).
18. Y. Iwasawa, *X-Ray Absorption Fine Structure for Catalyst and Surfaces*, World Scientific, Singapore (1996).
19. G. J. Colpas, M. J. Maroney, C. Bagyinka, M. Kumar, W. S. Willis, S. L. Suib, N. Baidya, and P. K. Mascharak, *Inorg. Chem.*, **30**, 920 (1991).
20. J. A. Victoreen, *J. Appl. Phys.*, **19**, 855 (1948).
21. I. Nakai and T. Nakagome, *Electrochem. Solid-State Lett.*, **1**, 259 (1998).
22. I. Nakai, K. Takahashi, Y. Shiraishi, T. Nakagome, F. Izumi, Y. Ishii, F. Nishikawa, and T. Konishi, *J. Power Sources*, **68**, 536 (1997).
23. A. Rougier, C. Delmas, and A. V. Chadwick, *Solid State Commun.*, **94**, 123 (1995).
24. R. D. Shannon, *Acta Crystallogr.*, **A32**, 751 (1976).
25. A. N. Mansour, J. McBreen, and C. A. Melendres, *J. Electrochem. Soc.*, **146**, 2799 (1999).
26. W. E. O'Grady, K. I. Pandya, K. E. Swider, and D. A. Corrigan, *J. Electrochem. Soc.*, **143**, 1613 (1996).